



1 SAO, AO, QBO, and Long-term trend of the peak OH airglow 2 emission

3 Sheng-Yang Gu^{1*}, Dong Wang¹, Liang Tang², Yafei Wei¹

4

5 ¹Electronic Information School, Wuhan University, Wuhan, China.

6 ²School of Optoelectronic Engineering, Chongqing University of Posts and Telecommunications, Chongqing, China.

7 *Corresponding author: Sheng-Yang Gu, (gushengyang@whu.edu.cn)

8

9 **Abstract.** Based on the volume emission rate of the OH airglow observed by TIMED/SABER, we fitted the peak emission
10 rate and the peak height of the OH airglow and analyzed the seasonal and interannual variations of both. The results show
11 similar latitudinal variations in the semiannual oscillation (SAO) and annual oscillation (AO) of peak emission rate and peak
12 height: the amplitude of SAO is greatest in equatorial regions and AO is greatest in mid-latitudes. For interannual variations,
13 we find that OH airglow emission in equatorial regions is modulated by the quasi-biennial oscillation (QBO), while the QBO
14 signal at other latitudes is much weaker than in equatorial regions and can be ignored. The QBO in OH airglow is consistent
15 with the phase variation of the QBO in the tropical lower stratosphere (30km), which is also consistent with the phase variation
16 of the QBO in the migrating diurnal tide. As an important kinetic process affecting OH airglow emission, we suggest that the
17 tides play an important role in the modulation of the OH airglow by the QBO. In addition, we have analyzed the relationship
18 between peak OH airglow emission and solar activity. The results show a good correlation between peak emission rate and
19 solar activity, with a correlation coefficient of 0.89, while peak height shows no significant solar cycle variation, with a
20 correlation coefficient of -0.66. The modulation of peak emission rate by solar activity has significant latitudinal variation.
21 The modulation effect is weakest in the equatorial region and greatest at mid-latitudes in both hemispheres.

22 1 Introduction

23 Airglow is the product of photochemical processes in the middle and upper atmosphere, and its radiation intensity is related to
24 atmospheric temperature and atmospheric density. At the same time, its time and space distribution is modulated by various
25 atmospheric dynamics processes such as atmospheric gravity waves, tidal waves, and planetary waves. As the radiation of the
26 atmosphere itself, airglow carries rich information about the middle and upper atmosphere and can be used as a medium to
27 study various dynamics and photochemical processes in the middle and upper atmosphere. The mesosphere/low thermosphere
28 (MLT) region, where complex optical phenomena and dynamical processes exist, is a key middle and upper atmosphere study
29 region. The OH Meinel airglow, one of the most intense airglow emissions in the nightglow, is located near an altitude of



30 about 87 km. By studying the variation of OH airglow emission, the study of various photochemical and kinetic processes as
31 well as matter and energy transport processes in the MLT region can be realized.

32 The changing characteristics of the OH airglow have been studied for a long time. Whether using ground-based observations
33 or satellite remote sensing observations, there have been many studies on the seasonal variation of OH airglow intensity. Abreu
34 and Yee (1989) analyzed the nighttime patterns of OH(8-3) airglow measured on the Atmosphere Explorer E satellite and find
35 that the diurnal variation of hydroxyl emissions is a function of latitude and season. They also observed strong semiannual
36 oscillation with a maximum near the equator. Takahashi et al. (1995) measured the OH airglow using a ground-based
37 multichannel airglow photometer at Fortaleza (3.9°S, 38.4°W) and found that the OH airglow intensity shows semiannual
38 oscillation, with a maximum at the equinoxes and a minimum at the solstices. Zaragoza et al. (2001) used OH airglow data
39 measured by ISAMS on the URAS satellite and found significant semiannual variations at low latitudes, especially at equatorial
40 regions, and annual variations at higher latitudes. Lopez-Gonzalez et al. (2004) analyzed more than 3 years of OH(6-2) airglow
41 observations at the Sierra Nevada Observatory (37.06°N, 3.38°W) and found that the amplitudes of annual and semiannual
42 variations in OH emission rates were comparable. Buriti et al. (2004) analyzed the intensity data of OH(6,2) airglow radiation
43 observed at equatorial stations from 1998 to 2001 and found a half-yearly cycle of variation. The maximum value of airglow
44 intensity appears at the equinoxes and the minimum value appears at the solstices. They suggest that atmospheric tidal
45 oscillations play an important role in the observed semiannual oscillation. Taylor et al. (2005) found semiannual oscillations
46 in mesospheric temperature and the intensity of the OH(6,2) and O₂(0,1) airglow using 25 months of Maui (20.8°N, 156.2°W)
47 mesopause thermometer (MTM) observations, and that the spring perturbation was also greater than in autumn. Shepherd et
48 al. (2006) analyzed the seasonal variations of O(1S) and OH(8,3) nightglow from data obtained by the Wind Imaging
49 Interferometer on UARS (WINDII) and found a strong semiannual variation dominating at the equator, which is thought to be
50 driven by the semiannual variation of diurnal tidal amplitudes, with tidal modulation also present in the annual variation at
51 mid-latitudes. Gao et al. (2010) used the OH airglow emission data from TIMED/SABER observations to analyze which
52 oscillations dominate the OH airglow emission and the distribution of these oscillations. Strong semiannual oscillations in the
53 OH airglow emission in the equatorial region have been observed using different observational methods. The maximum value
54 of OH airglow emission in the equatorial region occurs at the equinox and the minimum value occurs at the solstice. With
55 increasing latitude, annual oscillation dominates at higher latitudes.

56 Not only about the seasonal variation of OH airglow emission but also about the long-term variation of OH airglow emission
57 has made great progress. Wiens and Weill (1973) analyzed the diurnal, annual, and solar cycle variations of OH airglow by
58 studying OH airglow intensity data observed by filter photometers in the tropics and at latitude stations in the northern and
59 southern temperate zones. They found that the diurnal variation pattern is a function of latitude and season, and indicated that
60 the OH airglow intensity is influenced by solar activity. Batista et al. (1994) found a positive correlation between the OH(9,4)
61 airglow intensity obtained in Brazil (23° S, 45° W) and the F_{10.7} index by analyzing the relationship between this intensity and
62 the intensity of solar activity. Liu and Shepherd (2006) analyzed the relationship between OH airglow emission and solar
63 radiation using the WINDII observation data from 1991 to 1997 and pointed out that OH airglow emission is dependent on



64 solar radiation. Baker et al. (2007) found that the experimental data from SABER for several years exhibited equatorial
65 enhancements of the nighttime mesospheric OH airglow layer consistent with the high average diurnal solar flux. Pertsev and
66 Perminov (2008) analyzed the response of hydroxyl airglow to solar activity using observations from the Zvenigorod
67 Observatory (56° N, 37° E) and found that the response of emission intensity to the variation of F_{10.7} solar radio flux was 30%-
68 40%/100sfu, with a more significant response in winter compared to summer. Reid et al. (2014) analyzed hydroxyl (OH)(8-3)
69 airglow data obtained from filter photometer measurements near Adelaide, Australia. The results show that the OH airglow
70 intensity is related to solar activity. Many studies have shown that the intensity of OH airglow is closely related to solar activity,
71 but the emission height of OH airglow shows a different response. Von Savigny (2015) analyzed the vertical volume emission
72 rate of OH(3-1) airglow observed by the Scanning Imaging Absorption Spectrometer of the Atmosphere (SCIAMACHY) on
73 the Envisat satellite and found no significant solar cycle signature for the OH emission height. Gao et al. (2016) used the
74 airglow data observed by SABER to analyze the response of NO, O₂, 2.0 μm and 1.6 μm OH airglow to solar radiation, and
75 they found that the intensity and peak emission rate of the four airglow emissions were strongly correlated with solar radiation,
76 but the response of NO, 1.6 μm and 2.0 μm OH airglow peak heights to solar radiation was not significant. They also pointed
77 out that the response of airglow emission to solar radiation varies with latitude.

78 Numerical models are often analyzed in conjunction with observational data to study the relationship between OH airglow
79 radiation changes and dynamical processes and solar activity changes. Yee et al. (1997) analyze three-day observations from
80 the High-Resolution Doppler Imager (HRDI) instrument on UARS and simulations from the Thermosphere-Ionosphere-
81 Mesosphere-Electrodynamics General Circulation Model (Time-GCM). They show that the vertical motion, driven mainly by
82 tides, changes the atomic oxygen profile, leading to changes in the observed peak height and brightness of the airglow. The
83 upward motion reduces the atomic oxygen concentration at the top height of the mesosphere, thus reducing the OH airglow
84 intensity. Marsh et al. (2006) examined the variations of OH Meinel airglow by comparing SABER measurements of OH
85 airglow with predictions from a three-dimensional chemical kinetic model. They found that migrating diurnal tides have a
86 considerable influence on diurnal and seasonal variations at low latitudes, while at high latitudes the annual variations in
87 emissions are mainly due to the transport of oxygen by the seasonally reversed mean circulation. Huang (2016) used OHCD
88 and MACD models to simulate OH airglow and O airglow to study the effects of CO₂ gas concentration variation and solar
89 cycle variation on airglow intensity and volume emission rate (VER). The results show that the effect of solar cycle variation
90 on airglow variation is greater than the effect of CO₂ gas concentration variation on airglow variation.

91

92 Much progress has been made in the study of the seasonal and long-term variations of the OH airglow and the global
93 distribution characteristics of the amplitude and phase of the variations, but many details of these variations have not yet been
94 fully described. In addition to OH airglow intensity, peak emission rate and peak height are important parameters that can be
95 used to describe the airglow emission rate. OH airglow can provide important information for the study of mesospheric
96 dynamics and chemistry, and its long-term variation may be modulated by the cyclic variation of solar activity in addition to
97 the dynamics. Studying the seasonal and annual variation of OH airglow emission in the MLT region and the possible



98 modulation of OH airglow emission by solar activity can help advance the understanding of the underlying processes of energy,
99 chemistry, dynamics, and transport in the mesosphere and low thermosphere.
100 In this paper, we fit the OH airglow emission rates observed by SABER during 2002-2022 to obtain the peak emission rates
101 and peak heights and use them as parameters to describe OH airglow emissions. The seasonal and interannual variations of
102 OH airglow peak emission rate and peak height are analyzed. The data and analysis methods are presented in Section 2. Section
103 3 analyzes the semiannual, annual, and interannual variation of the peak emission rate and the peak height of OH airglow. For
104 seasonal variations, the SAO and AO of the peak OH airglow emission are analyzed, and the amplitudes and phases of the
105 SAO and AO are calculated and compared for different latitudes. For interannual variation, the correlation between the QBO
106 of peak OH airglow emission in the equatorial MLT region and the QBO of stratospheric zonal winds, as well as the influence
107 of peak emission rate and peak height by solar activity, are discussed, and the possible reasons for this phenomenon are
108 analyzed. An overview is given in Section 4.

109 2 Data and Analysis Method

110 2.1 TIMED/SABER

111 The Sounding of the Atmosphere using Broadband Emission Radiometry (SABER) instrument is one of four instruments on
112 NASA's TIMED (Thermospheric Ionospheric Mesospheric Energy Dynamics) satellite. SABER makes global measurements
113 of the atmosphere by using a broadband limb-scanning infrared radiometer that measures not only the volumetric mixing ratios
114 of O₃, CO₂, H₂O, [O], and [H], but also the NO OH emissions in the excited state. The wavelengths of the OH airglow emission
115 centers measured by SABER are 2.0 μm and 1.6 μm. The 2.0 μm channel measures the radiation to come from the OH (9, 7)
116 and OH (8, 6) bands, while the 1.6 μm channel measures the radiation from the OH (5, 3) and OH (4, 2) bands and part of the
117 OH (3, 1) band.

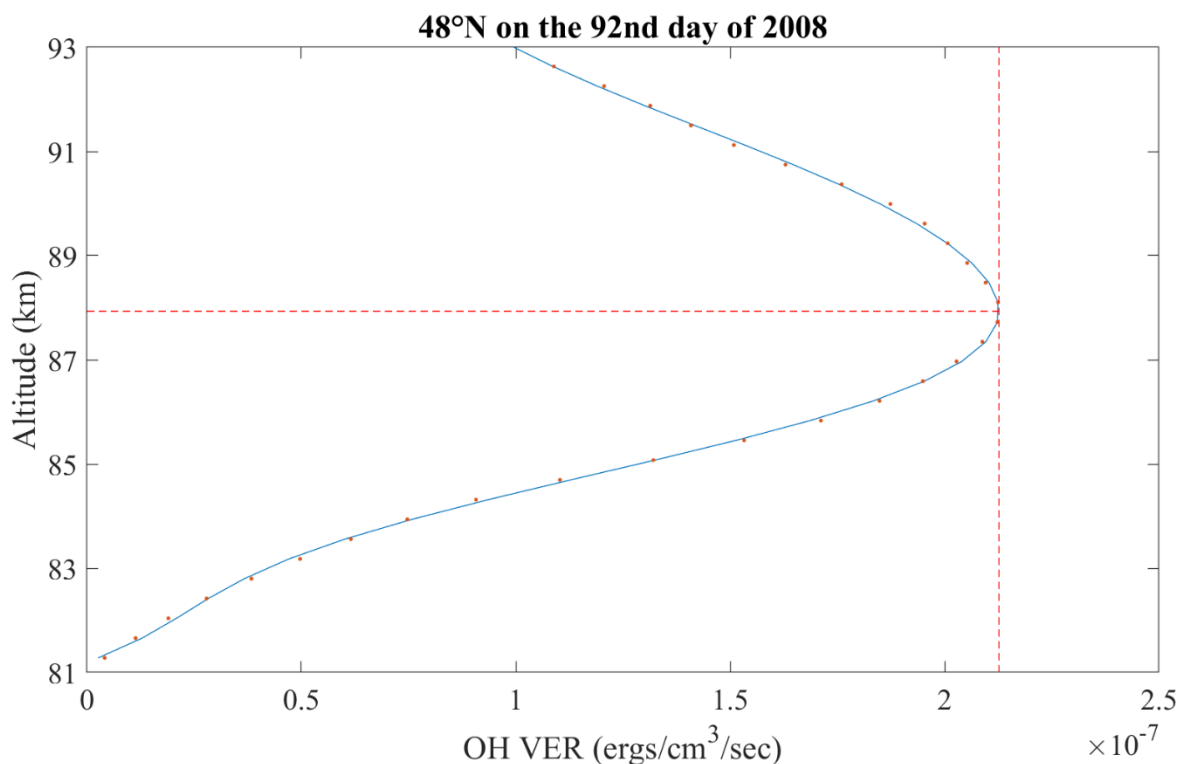
118 We use version 2.0 of the 1.6 μm OH data observed by bandpass filters with a central wavelength of 1.6 μm from January 25,
119 2002, to December 31, 2022. SABER can observe the latitude range from 53° in the winter hemisphere to 83° in the summer
120 hemisphere. To ensure data continuity at high latitudes and avoid inconsistent analysis due to missing measurements at high
121 latitudes, we chose to analyze OH airglow emission in the latitude range of 52.5°N-52.5°S. Before analyzing the long-term
122 variation of OH airglow peak emission rates and heights, we need to extract them from the height profiles of OH airglow
123 volume emission rates. The peak height of OH airglow emission falls mainly in the range of 80km to 90km, so we use the
124 Fourier fourth-order fitting method for the observation points near this range:

$$125 V(z) = a_0 + \sum_{i=1}^4 [a_i \cos(i * \omega * z) + b_i \sin i * \omega * z], \quad (1)$$

126 where z is the height and V is the OH airglow emission rate, resulting in the peak OH airglow emission rate and peak height,
127 which are expressed as peak emission rate and peak height, respectively, in the later paper. It is used to carry out the study of
128 seasonal and interannual variations of peak OH airglow emission. Figure 1 shows an example of the observed and fitted height



129 profile of the OH airglow volume emission at 48°S on April 1, 2008. The dashed lines in the figure point to the peak emission
130 rate (V_{\max}) and peak height (H_{\max}), respectively.
131



132
133 **Figure 1: Observations (points) and fitted curves (solid lines) of OH airglow emission on April 1, 2008, where the units of V_{\max} and**
134 **H_{\max} are ergs/cm³/sec and km, respectively.**

135 2.2 LRO

136 The low-resolution OMNI (LRO) dataset consists mainly of hourly averaged near-Earth solar wind magnetic and plasma
137 parameters from several spacecraft in geocentric or L1 (Lagrange point) orbit. LRO provides proton fluxes with energies above
138 1, 2, 4, 10, 30, and 60 MeV from several IMP and GOES spacecraft, and provides a wide range of geomagnetic and solar
139 activity indices. In this paper, the solar radiation flux $F_{10.7}$ provided by it from 2002 to 2022 is mainly used as an indicator of
140 the solar activity intensity.

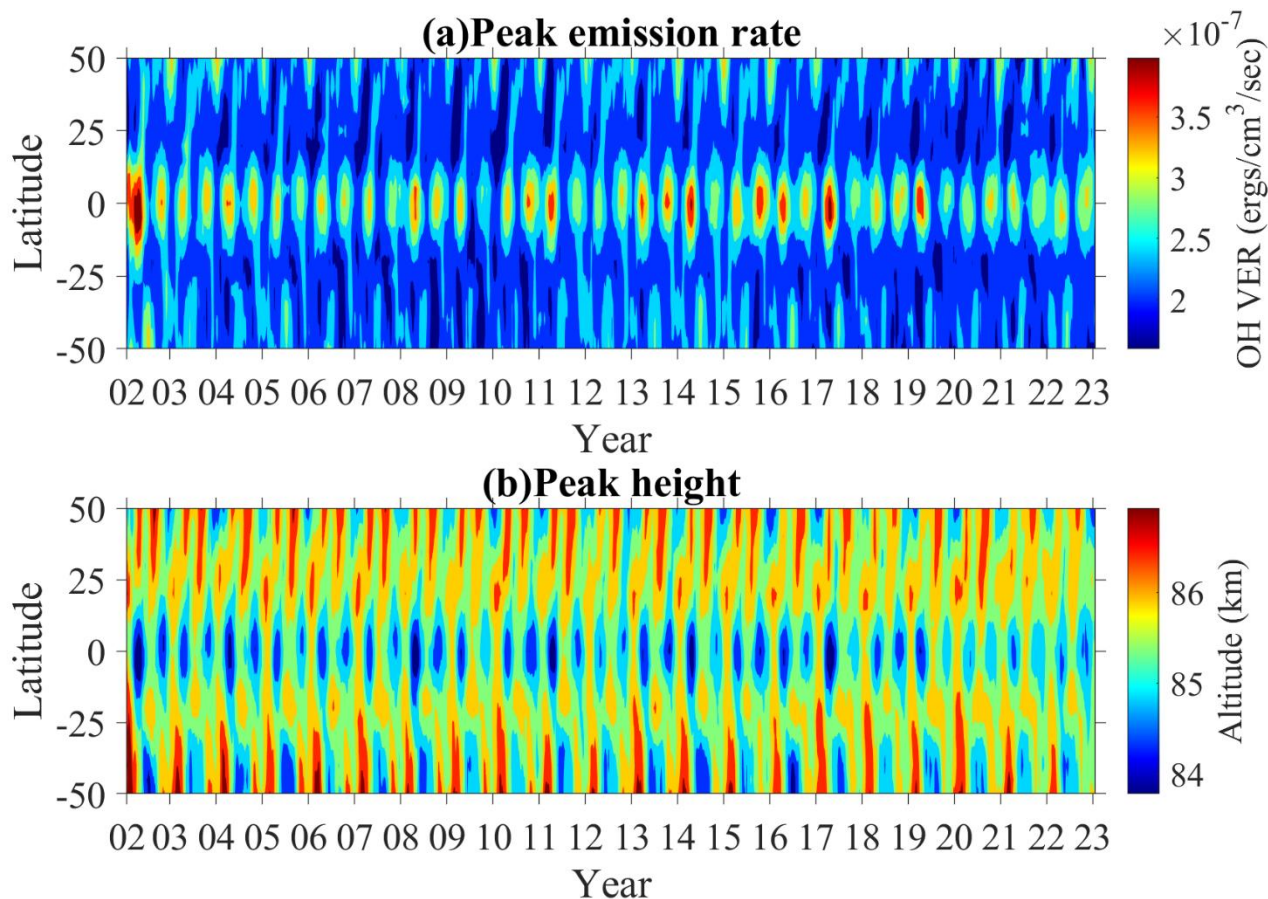


141 **2.3 MERRA2**

142 The second Modern-Era Retrospective analysis for Research and Applications (MERRA-2) is a NASA atmospheric reanalysis
143 using version 5.12.4 of the Goddard Earth Observing System Model Version 5 (GEOS-5), which enables the use of newer
144 microwave sounders and hyperspectral infrared radiance instruments, as well as other data types. Unlike MERRA, all data sets
145 for MERRA-2 are available on the same horizontal grid. This grid has 576 points in the longitudinal direction and 361 points
146 in the latitudinal direction, corresponding to a resolution of $0.625^\circ \times 0.5^\circ$. The vertical resolution of the data is changed from
147 0.667° in MERRA and the latitudinal resolution remains the same (0.5°). Their wind field data contain up to 80 km of zonal
148 wind data with a temporal resolution of 3 hours. We chose to characterize the equatorial stratospheric QBO using zonal winds
149 at 30km in the Singapore region ($0.625^\circ\text{N}, 103.125^\circ\text{S}$).

150 **3 Results and Discussion**

151 A grid of 5° latitude \times 1 day was constructed to study the long-term variation of OH airglow. The peak emission rate and peak
152 height obtained from the fit were first averaged daily and latitudinally. The averaged results were averaged by latitude range
153 and the result obtained by averaging was used as the value of the grid centroid. In the latitude direction, a total of 21 latitude
154 windows are obtained from 52.5°S to 52.5°N . The TIMED satellite needs to operate for about 60 days to cover the global 24h
155 place time with its measurements, and the results after the day averaging are smoothed with a sliding step of 1 day and a
156 window length of 60 days. The smoothed results are shown in Figure 2.



157

158 **Figure 2:** (a) Latitude-time distribution of peak emission rate. (b) Latitude-time distribution of peak height. The units are ergs/cm³/sec
 159 and kilometers, respectively. Peak emission rate and peak height are averaged over days and smoothed over a window length of 60
 160 days. The period starts from January 25, 2002, until December 31, 2022.

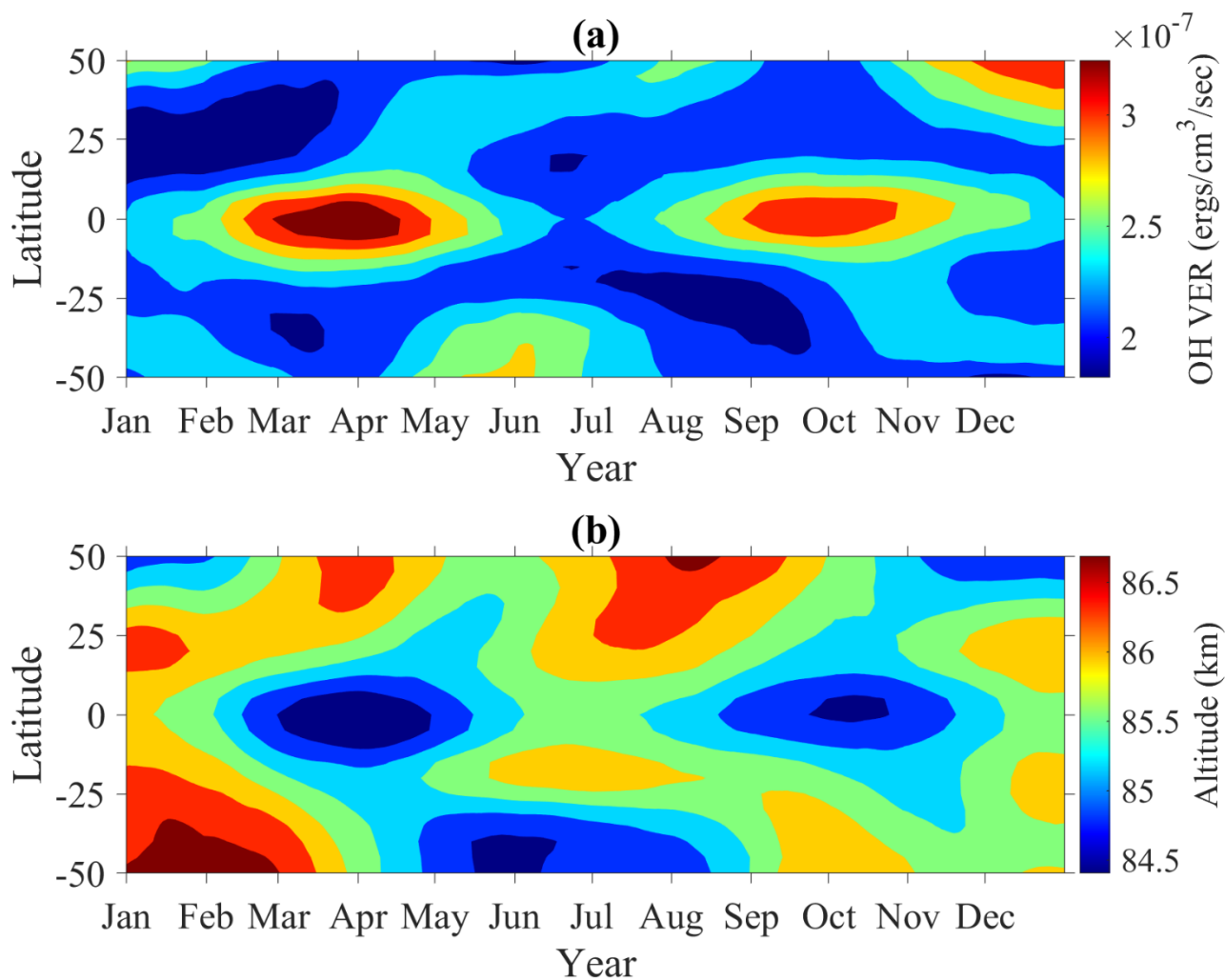
161 **3.1 Annual and Semiannual Oscillation**

162 In Figure 2, the strongest semiannual oscillations can be observed in the equatorial region, which is consistent with the results
 163 observed in the ground experiment of Taylor et al. (2005). To facilitate the study of annual and semiannual oscillation of
 164 airglow radiation, airglow radiation data for a total of 21 years from 2002 to 2022 are averaged by superimposing them. A
 165 superimposed year is obtained that can be used to represent a multi-year average of peak emission rate and peak height. Figure
 166 3(a) shows the peak OH airglow emission rate after multi-year averaging, and it can be seen that there is a clear semiannual
 167 oscillation in the equatorial region. The maximum value is at the equinox and the minimum value is at the solstice, and the
 168 extreme value at the September equinox is larger than that at the March equinox, which is consistent with the previous studies
 169 (Mulligan et al., 1995; Takahashi et al., 1995; Buriti et al., 2004).

170 Figure 3(b) shows the OH airglow peak height after multi-year averaging, and the same as the peak emission rate, the peak
 171 height has the same semiannual oscillation phenomenon, and the minimal value appears at the equinoxes. OH airglow peak



172 height is inversely proportional to the peak emission rate. In the equatorial region, the minimum value of the peak height at
 173 the equinox corresponds to the maximum value of the peak emission rate. The same phenomenon has been identified in
 174 previous studies and is thought to be the role of tides in this (Yee et al., 1997; Melo et al., 1999).



175

176 **Figure 3: A superimposed year of peak OH airglow emission. (a) Latitude-time distribution of the peak emission rate averaged over**
 177 **multiple years. (b) Latitude-time distribution of the peak height averaged over multiple years.**

178 In order to obtain the amplitudes and phases of SAO and AO in the peak OH airglow emission, a harmonic fitting method was
 179 used, applying the following Eq. (2):

180
$$f = f_0 + a * \cos\left(\frac{2\pi}{183(\text{day})}(t - t_{SAO})\right) + b * \cos\left(\frac{2\pi}{365(\text{day})}(t - t_{AO})\right), \quad (2)$$



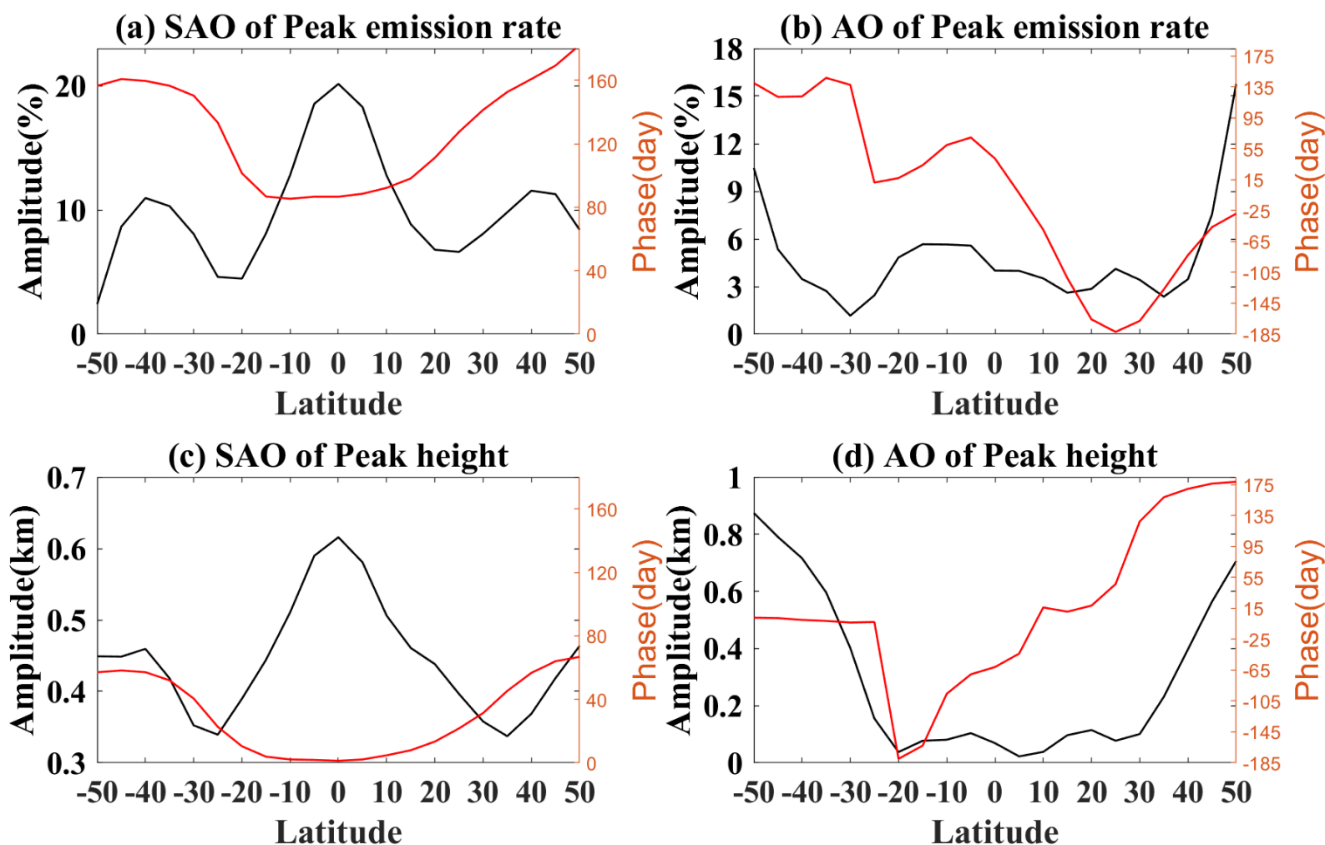
181 where f can be either the peak emission rate or the peak height, f_0 denotes the multi-year average, t is the time index in days,
182 and a and b are the amplitudes of SAO and AO. t_{SAO} and t_{AO} are the times at which the semi-annual and annual oscillation
183 maxima occur. Figure 4 shows the amplitudes and phases of the annual and semiannual oscillation of OH airglow peak
184 emission rate and peak height at different latitudes, respectively.

185 Figures 4 (a) and (b) show the latitudinal variation of peak emission rate relative amplitude in percentage terms: $(a/f_0) \times 100\%$,
186 $(b/f_0) \times 100\%$. As seen in Figure 4(a) SAO amplitudes range from 2% to 20% with three peaks, with the largest amplitude of
187 about 20% in the equatorial region. The phase of SAO is delayed from near day 90 (near the equinox) at the equator and then
188 with increasing latitude to near the solstice at 50°N/S. The peak emission rate has its largest amplitude during the equinox,
189 which is consistent with diurnal tides (Burrage et al., 1995). The peak emission rate is associated with diurnal tides and its
190 seasonality is likely to be caused by the seasonal variation of diurnal tides. Notably, the OH airglow peak emission rate in
191 Figure. 2 is anomalous in 2015, with the maximum value at the March equinox being smaller than the maximum value at the
192 September equinox, the reason for this occurrence we analyze later.

193 As shown in Figure 4(b), the amplitude of AO ranges between 1% and 16% with two weak peaks at 5°S and 25°N. There are
194 three troughs at 30°S, 15°N, and 35°N, respectively. In the latitude range of 30°-50°, the AO amplitude increases with
195 increasing latitude. The largest amplitude is found at 50°N/S, where the amplitude reaches 16% at 50°N and is greater than
196 11% at 50°S. Observing the AO phase, the amplitude of 25°N is greatest on day 183 of the first year, delayed towards the
197 poles. The amplitude of the 50°S reaches its maximum on day 140 of the second year and the 50°N reaches its maximum on
198 day 337 of the first year. Comparing the amplitudes of SAO and AO, we find that semiannual oscillation dominates at low
199 latitudes and annual oscillation is more frequent at higher latitudes.

200 We note the semiannual and annual variations in OH airglow intensity provided by Reid et al. (2014), who analyzed filter
201 photometer measurements at Buckland Park (34.6°S,138.6°E). They found a value of 7% for SAO, which peaked at day 160
202 and was in good agreement with our SAO results. The AO is a poorer match, with Reid's amplitude of 14%, several times that
203 of our results. The phase shows a maximum amplitude at day 159, in general agreement with our results.

204 The amplitude of the peak height is the absolute amplitude rather than the relative amplitude, as shown in Figure 4(c), and the
205 trend of the phase and amplitude change of the peak height SAO is the same as that of the peak emission rate SAO. The SAO
206 amplitude is between 0.3 and 0.6 km. It has three peaks at 40°S, 0° and around 50°N, the equatorial peak being the strongest.
207 The AO amplitude is below 1km, and the two weak peaks at 5°S and 20°N are significantly lower than those at higher latitudes.
208 At low latitudes, the strongest variation in peak height is SAO; near 50°, AO is the strongest. The phase of SAO in peak height
209 is delayed from near the solstice at the equator to near the equinox at 50°S (from the winter solstice to the following equinox).
210 Observing the AO phase, the amplitude of 20°S is greatest on day 186 of the first year, delayed towards the poles. The
211 amplitude of 50°S reaches its maximum amplitude on day 2 of the second year and the 50°N reaches its maximum on day 178
212 of the second year. The amplitude and phase variations of SAO are consistent with the results of Gao et al. (2010), but the
213 results of the AO differ from ours.



214

215 **Figure 4:** (a) Latitudinal distribution of amplitude and phase of SAO in the peak emission rate. (b) Latitudinal distribution of
 216 amplitude and phase of AO in the peak emission rate. (c) Latitudinal distribution of amplitude and phase of SAO in the peak height.
 217 (d) Latitudinal distribution of amplitude and phase of AO in the peak height.

218 3.2 Modulation by QBO

219 The production of hydroxyl groups (OH*) is associated with the following reactions: $O_3 + H \rightarrow OH^* + O_2$. As a reaction
 220 product, the rate of OH* production is directly related to $[O_3]$ and $[H]$ and the rate of reaction depends on the local temperature
 221 and density. In addition, $[O_3]$ is proportional to $[O]$ under photochemical equilibrium conditions. Thus, OH emission is also
 222 related to $[O]$. The atomic oxygen distribution derived by Russell and Lowe (2003) using the hydroxyl emission and oxygen
 223 green line emission observed by WINDII exploits precisely the relationship between OH emission and atomic oxygen.

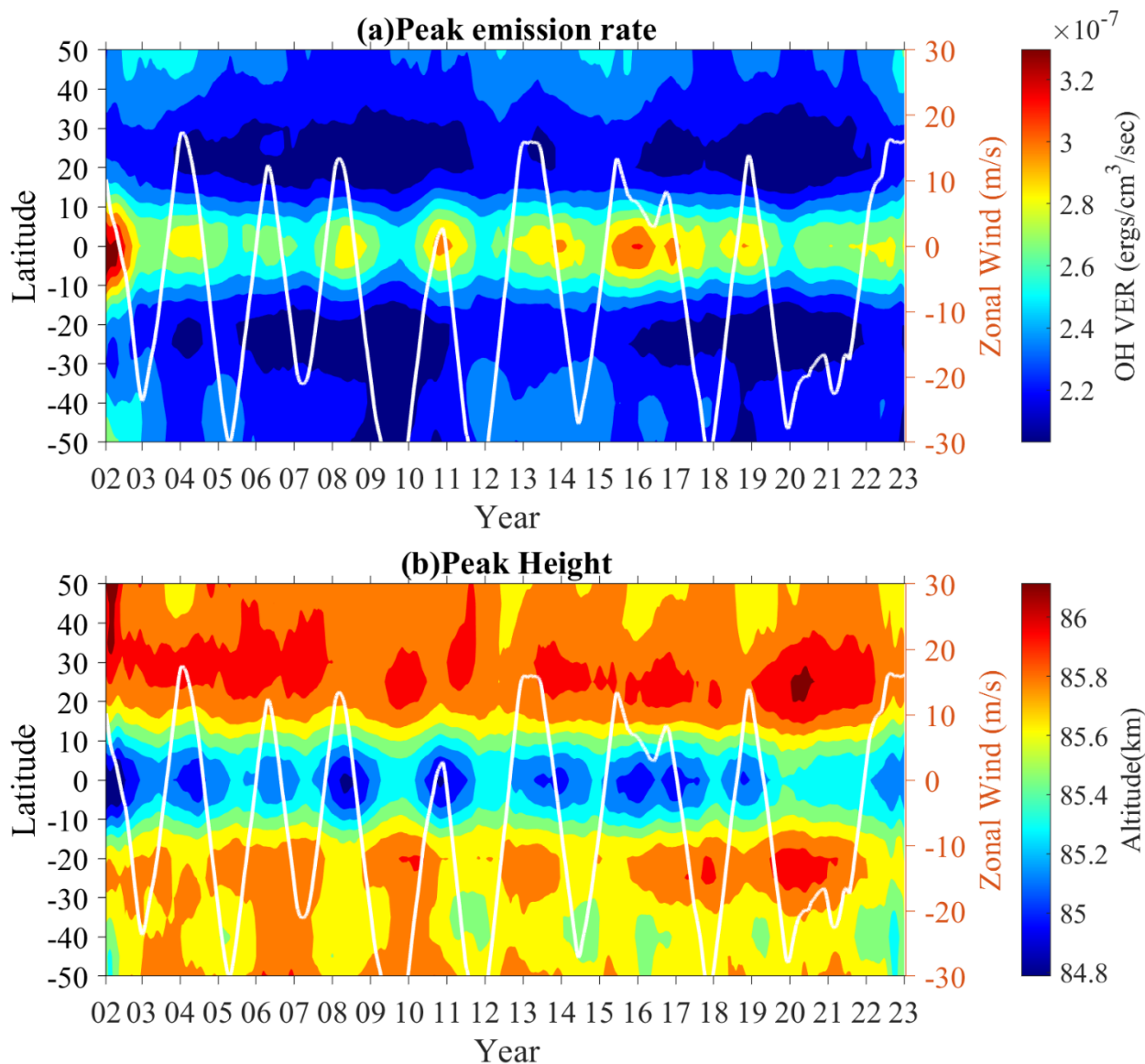
224 At low latitudes where SAO dominates the hydroxyl airglow emission, Burrage et al. (1996) analyzed horizontal wind field
 225 measurements obtained from 1992 to 1995 by the High-Resolution Doppler Imager experiment on UARS and found an
 226 oscillation with a period of about 2 years, with the maximum amplitude occurring near an altitude of 85 km, which corresponds
 227 to the peak height in our results. One of the mesospheric quasi-biennial oscillation (MQBO) shows a similar spatial distribution
 228 structure to the mesospheric semiannual oscillation (MSAO) and exhibits a phase relationship with the stratospheric quasi-



229 two-year annual oscillation, suggesting that the MSAO is modulated by the stratospheric quasi-two-year oscillation. In addition,
230 the Christmas Island MF radar (2°N, 130°W) also detects an MQBO with the same phase and the same peak height, although
231 the amplitude is only half of that shown by HRDI, this observation also confirms the existence of this MQBO.

232 To facilitate the analysis of the relationship between OH airglow emission and stratospheric QBO, we smoothed peak emission
233 rate and peak height with a window of 365 days in length, which avoids the effect of seasonal variations on the analysis of the
234 results.

235



236

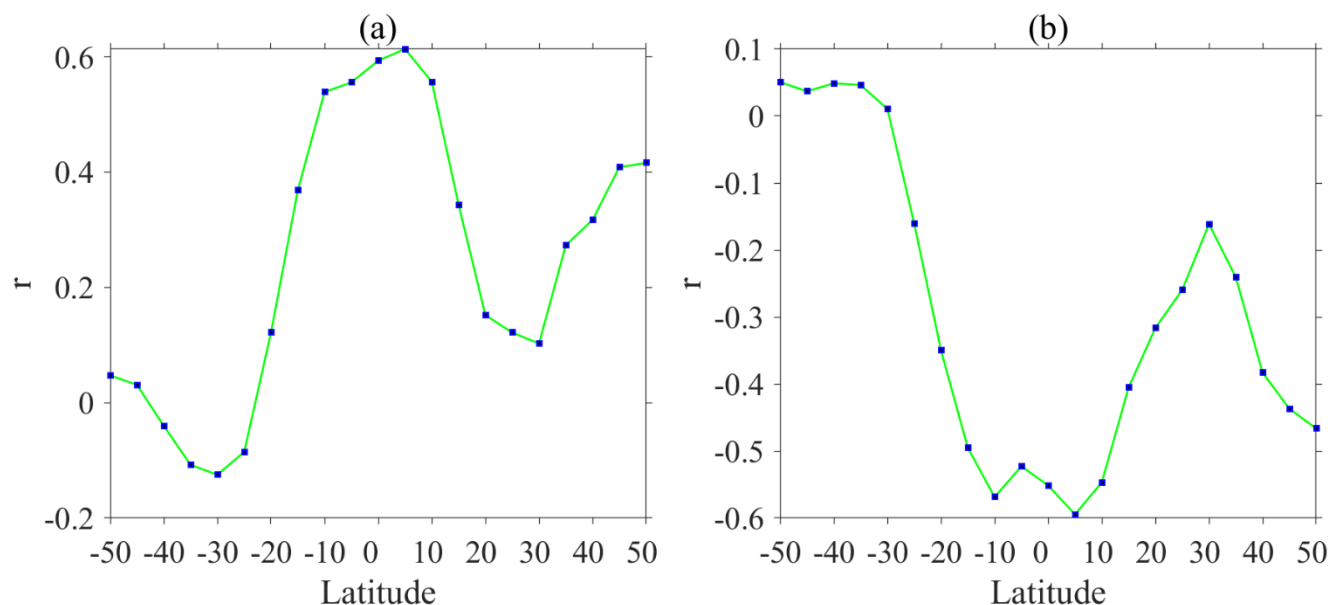


237 **Figure 5: (a) Latitude-time distribution of peak emission rates in $\text{ergs/cm}^3/\text{sec}$. Emission rates are smoothed over a window length of**
238 **365 days. The white line refers to the daily average of the equatorial stratospheric zonal winds, again smoothed over a window length**
239 **of 365 days. Eastward winds are indicated by positive values. (b) Same as (a) but for peak height.**

240 Figure 5(a) shows the latitude-time distribution of peak OH airglow emission rates, with the white line being the daily average
241 of the equatorial stratospheric zonal winds. After 365 days of smoothing, it can be observed that in the equatorial region, the
242 QBO signal in the OH airglow emission may be related to the QBO signal in the stratospheric latitudinal winds. The peak
243 emission rate QBO signal is much weaker in the higher latitude region than in the equatorial region, which is also consistent
244 with previous findings (Marsh et al., 2006; Shepherd et al., 2006). Observations of the phase of the peak emission rate in the
245 equatorial region show that the phase change of the emission rate is consistent with the phase change of the tropical zonal wind
246 at 30 km. The OH airglow emission rate is relatively high when the zonal winds are to the east, as in 2011. When the zonal
247 winds are westward, the OH airglow emission rate is relatively low, e.g. in 2010. It is worth noting that the anomalies in OH
248 airglow emission in 2015 mentioned above are associated with stratospheric QBO anomalies. The QBO anomalies in OH
249 airglow emission rate from 2015-2016 correspond to the anomalous changes in QBO observed by radio soundings by Newman
250 et al. (2016), which also confirms that OH airglow emission at 85 km is indeed affected by QBO in the tropical stratosphere
251 influence.

252 Figure 5(b) shows the latitude-time distribution of peak OH airglow heights, with the white line being the daily average of the
253 equatorial stratospheric zonal winds. In the equatorial region, the peak height is modulated by the QBO as is the peak emission
254 rate. Of course, since peak height is inversely proportional to peak emission rate, a high peak emission rate corresponds to a
255 low peak height. The QBO signal for peak height is also weak at higher latitudes. Peak heights show more short-period
256 variation, while peak emission rates show long-period variation, e.g. the peak emission rates in 2002 and 2014 are significantly
257 larger than that in 2008 and 2019, which we will analyze later.

258 The QBO signal in the equatorial region has been the subject of many related studies. Xu et al. (2009) analyzed the quasi-
259 biennial oscillation of the migrating diurnal tide based on data from TIMED observations. After comparison, we find that the
260 distribution of OH airglow emission at low latitudes is similar to that of the migrating diurnal tide in temperature. The QBO
261 phenomenon is more pronounced in equatorial regions compared to higher latitudes, due to the dominant tidal influence on
262 OH airglow emission at lower latitudes. Pramitha et al. (2021) found a good correspondence between the mesosphere-low
263 thermosphere diurnal tide and the stratospheric quasi-biennial oscillation (SQBO) based on meteor radar observations and
264 Whole Atmosphere Community Climate Model (WACCM) simulations. As to how stratospheric QBO modulates the emission
265 of OH airglow, Shepherd et al. (2006) found a decrease in the center of the airglow emission maximum during QBO modulation,
266 indicating the downward transport of atomic oxygen. This is also verified by the significant decrease in peak height in Figure
267 5(b) when the zonal wind is eastward compared to when the zonal wind is westward. They suggest that the tidal influence on
268 the mesospheric airglow emission is due to a corresponding tidal change in the atomic oxygen mixing ratio caused by vertical
269 motion. The stratospheric QBO phase variation is consistent with the tides in the MLT region and the airglow emission phase
270 variation. The QBO likely modulates the airglow emission at low latitudes through the tides.



271

272 **Figure 6: (a) Latitudinal dependence of the correlation coefficient between peak emission rate and QBO in the stratosphere; (b)**
 273 **Latitudinal dependence of the correlation coefficient between peak height and QBO in the stratosphere.**

274 To investigate the relationship between the peak OH airglow emission and the QBO of the tropical stratospheric atmosphere
 275 at different latitudes, we calculated the correlation coefficient between OH airglow and stratospheric QBO. Figure 6 shows the
 276 correlation with latitude, where Figure (a) shows the correlation between peak emission rate and stratospheric QBO, with the
 277 strongest correlation in the equatorial region with a correlation coefficient of 0.6. The comparison shows that the correlation
 278 is not the same in the two hemispheres. In the southern hemisphere, the correlation begins to weaken with increasing latitude,
 279 with a correlation coefficient of 0.12 at 20°S, and then becomes negative, with a correlation coefficient of -0.12 at 30°S. In the
 280 northern hemisphere, the correlation coefficient decreases with increasing latitude, with the smallest correlation coefficient of
 281 0.1 at 30°N. The correlation coefficient then increases with increasing latitude, with a correlation coefficient of 0.42 at 50°N.
 282 Figure (b) shows the correlation between the peak height and stratospheric QBO, similar to the peak emission rate in (a), and
 283 again the two are most correlated at the equator with a maximum correlation coefficient of -0.59. Comparing the two
 284 hemispheres, in the southern hemisphere the correlation is negative at latitudes greater than 30°. In the northern hemisphere,
 285 the absolute value of the correlation coefficient increases at latitudes greater than 30°. Comparing the different latitudes, we
 286 can find that the OH airglow emission responds most strongly to QBO in the equatorial region and is modulated by
 287 stratospheric QBO. As latitude increases, the QBO signal of OH airglow emission weakens. The modulation by QBO differs
 288 between the two hemispheres, with the correlation coefficient weaker in the southern hemisphere than in the northern
 289 hemisphere at the same latitude, especially at latitudes greater than 30°.

290



291 3.3 Modulation by Solar Activity

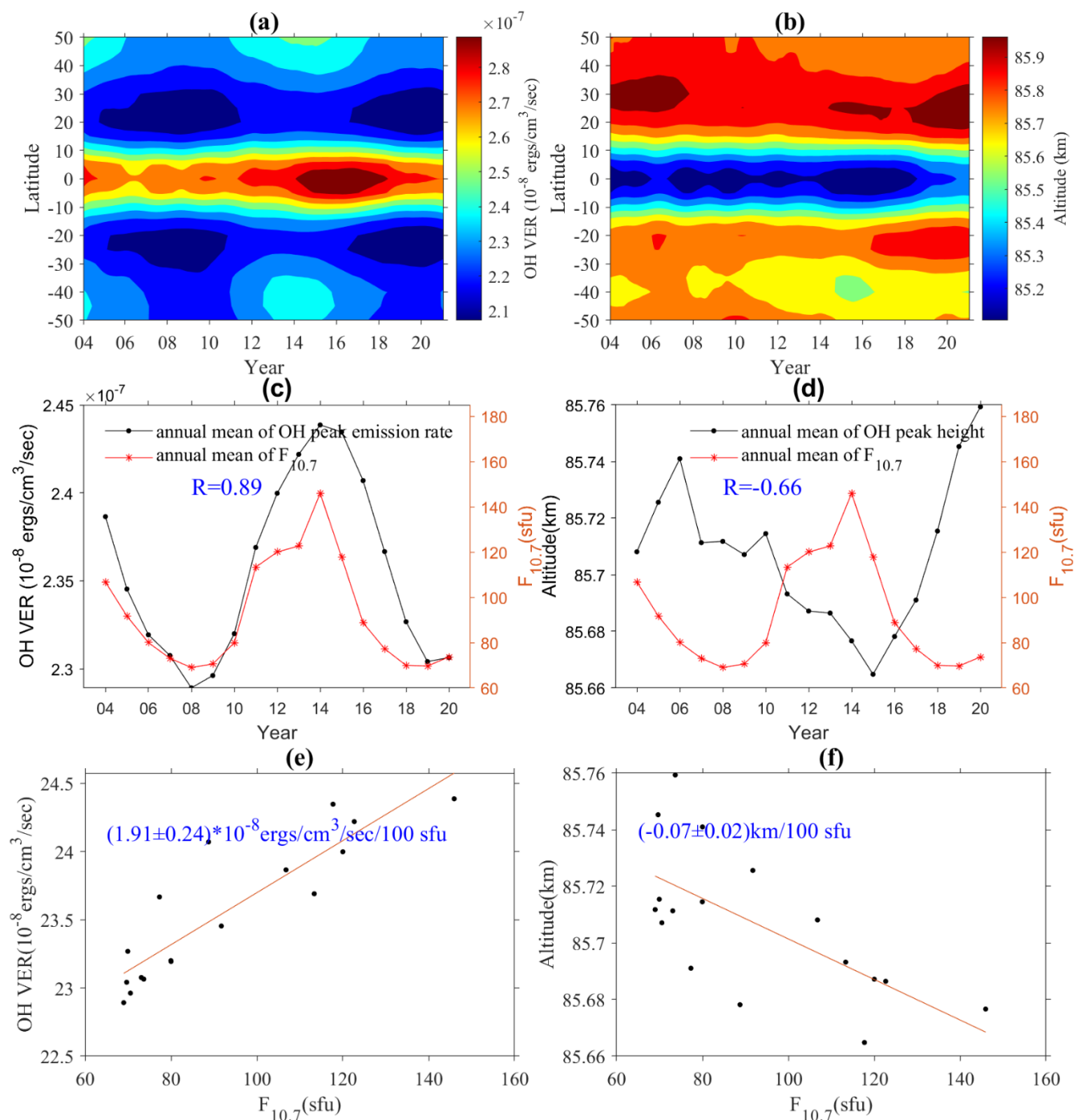
292 In addition to seasonal variations, at certain latitudes, e.g. around 50° latitude, the OH airglow appears to have a greater peak
293 emission rate during 2002-2003 and 2014-2015 than near 2008-2009 and 2019-2020. Airglow is very sensitive to atmospheric
294 conditions, and solar variations also affect atmospheric conditions such as temperature and gas concentration, with any change
295 in temperature or gas concentration leading to a change in airglow intensity. Since solar radiation directly drives the production
296 of atomic oxygen, then OH airglow emission is likely to vary with solar activity, i.e. it is modulated by solar activity. Scheer
297 et al. (2005) analyzed rotational temperature and airglow brightness variations in the OH (6-2) and O-2 (0-1) bands measured
298 at El Leoncito (32°S, 69°W) from 1998 to 2002 and found that at 87 km, there was no correlation with the solar radio flux,
299 while a very strong correlation developed at 95 km. This section investigates the correlation between peak global OH airglow
300 emission and solar activity by using SABER-sounding data and the 10.7 cm solar radiation stream ($F_{10.7}$) dataset.

301
302 On top of smoothing with a 365-day-long window, a three-year window was used and the smoothed results are shown in Figure
303 7(a) and Figure 7(b). $F_{10.7}$ data were smoothed in the same way, and to ensure consistency and accuracy of the smoothed results,
304 the first and last two years of data were removed, and we chose the data for the time range 2004 to 2020. Where (a) indicates
305 the latitude-time distribution of peak emission rate and (b) indicates the latitude-time distribution of peak height. As can be
306 seen from the results shown in Fig. 7(a), OH airglow emission rates are influenced by solar activity, with peak emission rates
307 significantly greater in high solar activity years such as 2014 than in low solar activity years such as 2008 and 2019. Notably,
308 the response of peak emission rate to solar activity in equatorial regions differs from that at higher latitudes, with an advance
309 in the response of OH airglow emission in 2008, a low solar activity year. The same phenomenon was found by Clemesha et
310 al. (2005) when they studied the monthly mean OH(6-2) band intensity at Cachoeira Paulista (23°S, 45°W) during the period
311 1987 to 2000. They found that the maximum intensity occurred about 1.4 years before the maximum of solar cycle 22. Deutsch
312 and Hernandez (2003) also found that the response of OI 558 nm to solar activity shows some lag, possibly because the decline
313 in emission intensity after the solar maximum is slower than the decline in solar activity. The peak height in Fig. 7(b) also
314 shows some response to solar activity but is significantly weaker than the response of the peak emission rate. Von Savigny
315 (2015) found no clear long-term trends or 11-year solar cycle features in the OH emission height time series.

316 Figure 7(c) shows the annual average change in OH airglow peak emission rate (black dot and line) over the period 2004-2020,
317 calculated from smoothed data. The trend in the global annual average of the peak emission rate closely matches the change
318 in $F_{10.7}$ (red star and line) shown in Fig. 7c, with a correlation coefficient of 0.89. These results suggest that the change in peak
319 OH airglow emission may be modulated by solar activity. Figure 7(d) shows the global annual mean variation in peak height,
320 from which we can see that the peak height, although showing an opposite trend to solar activity, has a correlation coefficient
321 of only -0.66, and the peak height is probably less influenced by solar activity.

322

323



324

325 **Figure 7: The interannual variations of peak OH airglow emission. (a) Latitude-time distribution of peak emission rates in**

326 **ergs/cm³/sec. Emission rates are smoothed over a window length of 3 years. (b) Latitude-time distribution of peak height in km. (c)**

327 **The global year average of peak emission rate and $F_{10.7}$ during 2004-2020. (d) The global year average of peak height and $F_{10.7}$ during**



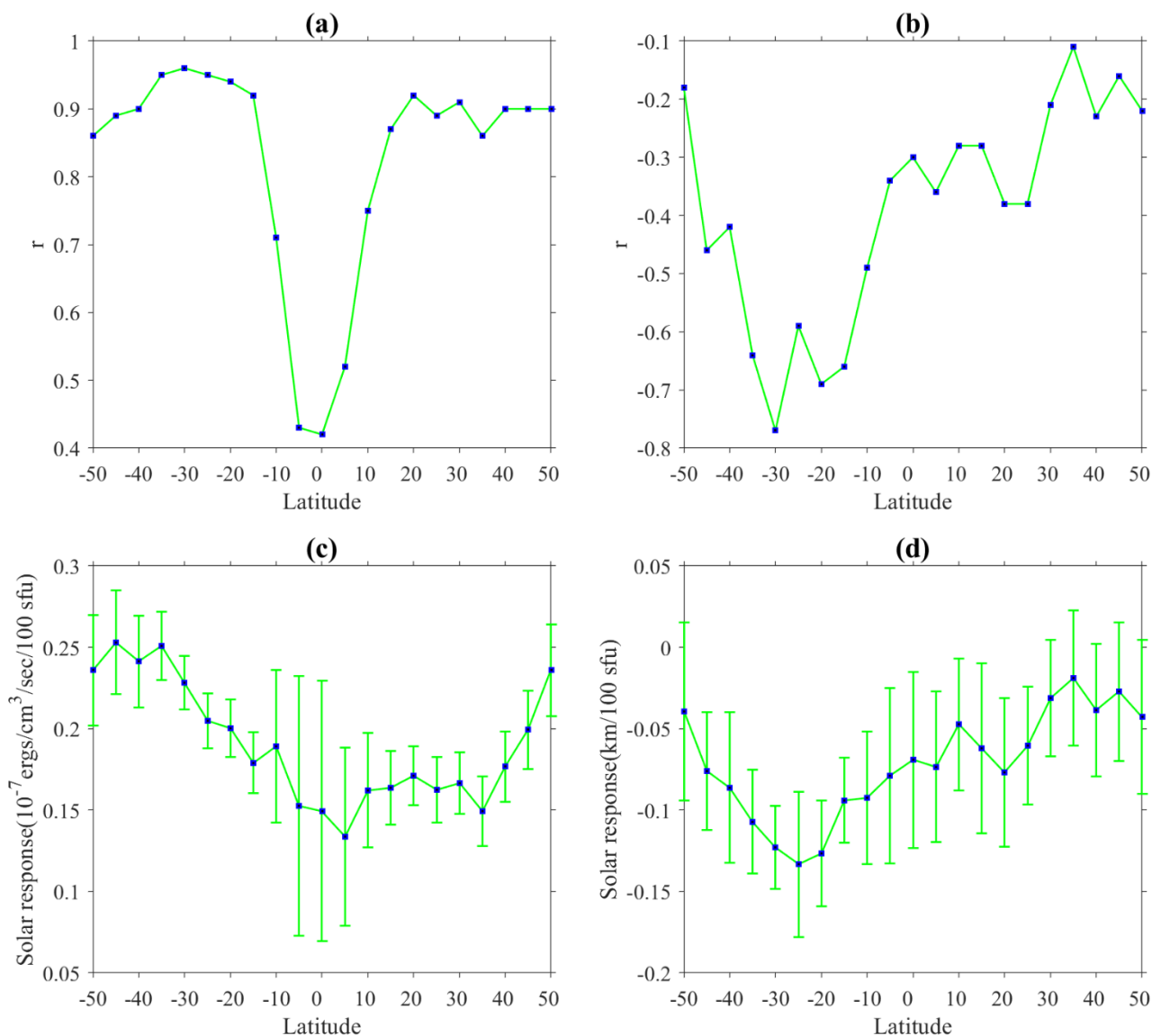
328 **2004-2020. (e) The scatterplot of $F_{10.7}$, peak emission rate, and the solar response value of peak emission rate. (f) The scatterplot of**
329 **$F_{10.7}$, peak height, and the solar response value of peak height.**

330 Analysis of the solar cycle dependence on the peak emission rate and its solar response. A global annual mean series scatter
331 plot between the OH airglow peak emission rate and $F_{10.7}$ is shown in Fig. 7(e), and that of the peak height is shown in Fig.
332 7(f). From Fig.7(e) and Fig. 7(f), we find a clear linear relationship between the OH airglow emission and the corresponding
333 annual average of $F_{10.7}$. Assuming a linear relationship, we use linear regression to calculate the solar response to OH airglow.
334 To investigate the solar activity dependence of the OH airglow. Using a linear approximate regression model for describing
335 the relationship between OH airglow and solar radiation flux $F_{10.7}$:

$$336 \quad f = A + B * F_{10.7} , \quad (3)$$

337 where B is the slope of the linear regression equation and A is its ordinate at the origin; that is, A is a constant and B is the
338 coefficient of linear fit derived from the least-squares regression analysis, representing the solar response to the OH peak
339 airglow emission rate. Using least-squares regression calculations, we obtain the global response of the OH peak airglow
340 emission rate to solar activity and its standard deviation. The solar response value for the peak emission rate is (1.91 ± 0.24)
341 $*10^{-8}$ ergs/cm³/sec/100 sfu as shown in Figure 7(e). The solar response value for the peak height is (-0.07 ± 0.02) km/100 sfu
342 as shown in Figure 7(f).

343 After analyzing the response of the global (50°S-50°N) mean of OH airglow emission to solar activity, the response of different
344 latitude zones to solar activity is analyzed below. A correlation analysis of the annual mean series for each latitudinal zone
345 yielded correlation coefficients between the peak emission and $F_{10.7}$ for 21 latitudinal zones, and the results are shown in Fig.
346 8(a). The correlation coefficients for the higher latitude zones are all greater than 0.6, except for the equatorial zone where the
347 correlation coefficient is only 0.42. The largest correlation coefficient is 0.96 for 30°S. Figure 8(b) shows the correlation
348 coefficients between peak height and $F_{10.7}$ for each latitude zone. The correlation coefficients are less than 0.6 for all latitude
349 zones except near 30°S where the correlation coefficient is greater than 0.6.



350

351 **Figure 8: The latitudinal dependence in the solar response of peak OH airglow emission. (a) The correlation coefficients between**
 352 **peak emission rate and $F_{10.7}$ for 21 latitude zones. (b) The correlation coefficients between peak height and $F_{10.7}$ for 21 latitude zones.**
 353 **(c) The solar response ranges of peak emission rate for 21 latitude zones, and the vertical bars show the standard deviation of solar**
 354 **response. (d) The solar response ranges of peak height for 21 latitude zones, and the vertical bars show the standard deviation of**
 355 **solar response.**

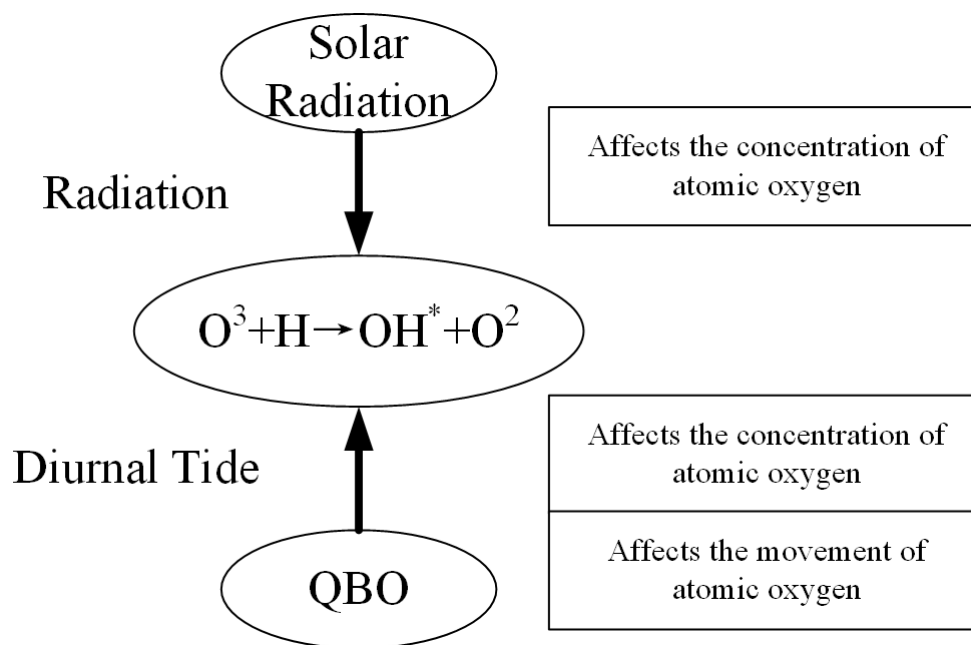
356 Using the least squares method, we obtained the latitudinal distribution of the peak emission rate response to solar activity and
 357 its standard deviation. Figure 8(c) shows the magnitude of the peak emission rate response to solar activity and its standard
 358 deviation for each latitude zone. The response amplitude is smallest at the equator and increases with increasing latitude. The
 359 solar response values range from a minimum of $0.14 \cdot 10^{-7}$ ergs/cm³/sec/100 sfu at the equator to a maximum of $0.24 \cdot 10^{-7}$



360 ergs/cm³/sec/100 sfu in the 50°S latitude zone. Figure 8(d) shows the magnitude of the peak height response to solar activity
361 at each latitude zone and its standard deviation. The response is weak at the equator and in the northern hemisphere, with the
362 strongest response near 25° in the southern hemisphere at -0.13 km/sfu. A comparison of the latitudinal distribution
363 characteristics of the solar response to OH airglow emission reveals that the solar response in the southern hemisphere is
364 greater than that at the corresponding latitude in the northern hemisphere. In each hemisphere, the standard deviation of the
365 solar response increases gradually from 30° to the equator and the poles. Tang et al. (2018), in using the SABER and F_{10.7}
366 datasets to study the correlation between peak emission rate and solar activity, found that peak emission rate was significantly
367 correlated with the solar cycle and that the correlation coefficient was also higher in the Southern Hemisphere than in the
368 corresponding latitudes in the Northern Hemisphere. In addition, the effects of planetary waves, tides, and the coupling between
369 them on airglow may vary with latitude and solar activity. A study by Laskar et al. (2013) showed that during periods of low
370 solar activity, the influence of the lower atmosphere on the upper atmosphere was found to be stronger. During periods of high
371 solar activity, there is a clear correlation between the behavior of the upper atmosphere and direct solar forcing, but the effect
372 of lower atmospheric wave activity on the upper atmosphere is weaker. Laskar et al. (2014) found that the effect of planetary
373 waves and the coupling of planetary waves and tides on the upper atmosphere varies with solar activity. These may also
374 contribute to the latitudinal dependence of the airglow response to solar activity.

375 Figure 9 illustrates the mechanism by which QBO and solar activity regulate OH airglow. Marsh et al. (2006) compared model
376 and observational data and found that most of the variability in OH airglow emission is caused by changes in the production
377 rate of ozone. At the height of the peak emission, the variation is mainly caused by changes in atomic oxygen due to vertical
378 transport. For QBO, we find that the phase variation of OH airglow emission in the equatorial region remains consistent with
379 the stratospheric QBO phase variation. Dynamic processes dominate the effect on the emission rate, and the increase in
380 emission rate is mainly caused by the increase in the mixing rate of atomic oxygen produced by downward tidal motion. As
381 the stratospheric zonal wind field moves eastward, the enhanced downward motion coincides with enhanced atomic oxygen
382 concentrations, enhanced OH airglow emission rate, and minimization of OH airglow emission height. We, therefore, speculate
383 that tides play an important role in the modulation of OH airglow emission by QBO. In terms of solar activity, the production
384 of atomic oxygen is influenced by solar radiation, so the OH airglow emission rate exhibits variations in the solar cycle. In
385 contrast, the variation in peak airglow height is mainly driven by tidal-driven vertical motion that changes the distribution of
386 atomic oxygen, so the variation in peak airglow height is less influenced by solar activity.

387



388

389 **Figure 9: Schematic representation of the mechanism by which OH airglow is modulated by QBO and solar activity.**

390 **4 Summary**

391 In this paper, based on the observed OH airglow emission data from the TIMED/SABER satellite from 2002-2022, the peak
 392 emission rate and a corresponding height of OH airglow were obtained by Fourier fitting method, and the seasonal and
 393 interannual variations of the peak emission rate and peak height were analyzed. For the seasonal variation, the peak emission
 394 rate and height were superimposed and averaged to observe the semiannual oscillation and annual oscillation of the peak
 395 emission rate and height. As a result, the latitudinal variations of peak emission rate and height were similar. The SAO
 396 amplitude ranges between 2% and 20% for peak emission rate, with the largest amplitude of about 20% in the equatorial region
 397 and two peaks larger than 40° N/S. The AO amplitude ranges between 1% and 16%, with two weak peaks at 10° S and 25° N,
 398 with the weakest peak at 25° N. The maximum value of the SAO amplitude occurs during the equinox, which is consistent
 399 with diurnal tides and verifies that the OH airglow emission is influenced by diurnal tides. The phase of the SAO is delayed
 400 from near the equinox at the equator to near the solstice at 50°S / N. For the phase of the AO in peak emission rate, the
 401 maximum amplitude first appears on day 183 of the first year at 25°N, delayed towards the poles. The maximum amplitude
 402 occurs at 50°S on day 140 of the second year and at 50°N on day 337 of the first year. For peak height, the SAO amplitude
 403 has three peaks, at 40° S, 0° and around 50° N, with the strongest peak at the equator. The AO amplitude has two weak peaks
 404 at lower latitudes at 5° S and 20° N, which are smaller than those at higher latitudes. The phase of the SAO at peak height is
 405 delayed from near the solstice at the equator to near the equinox at 50° N/S. For the phase of the AO in peak height, the AO is
 406 delayed from 20°S on day 186 of the first year to day 2 of the second year at 50°S and day 178 of the second year at 50°N.



407 Semiannual oscillations dominate at lower latitudes and, with increasing latitudes, annual oscillations dominate at higher
408 latitudes.

409

410 The OH airglow emission also shows a QBO signal for interannual variations, especially in the equatorial region. The peak
411 emission rate and height are smoothed so that the phase variation remains consistent with the stratospheric zonal winds. When
412 the wind field is to the east, the peak emission rate is relatively large and the peak height is relatively low. Comparing different
413 latitudes, we find that the correlation between the peak OH airglow emission and stratospheric QBO is strong in the equatorial
414 region, which is modulated by QBO, while the QBO signal is weak in other latitudes. OH airglow emission variation is
415 influenced by changes in atmospheric temperature and related atmospheric components, and as an important dynamic process
416 affecting OH airglow emission variation, migrating diurnal tides also have QBO. QBO in the stratosphere, QBO in the tide,
417 and QBO in the OH airglow emission have similar phase changes. Since the tidal influence on mesospheric airglow emission
418 is through the corresponding tidal change in the atomic oxygen mixing ratio caused by vertical motion, QBO likely modulates
419 airglow emission at low latitudes through tides.

420 In addition, the correlation between peak OH airglow emission and solar activity has been analyzed. The observed changes in
421 peak OH airglow emission rate correlate well with changes in solar activity over the period 2004-2020, with a correlation
422 coefficient of 0.89, while peak OH airglow emission heights show no significant solar cycle variations. We believe this may
423 be because the peak emission rate will be larger in years of high solar activity. After all, solar radiation affects the production
424 of atomic oxygen. However, the variation in peak airglow height is mainly driven by tidally driven vertical motions that alter
425 the distribution of atomic oxygen, and therefore the variation in peak airglow height is less influenced by solar activity. The
426 solar response of the global peak OH airglow emission is $(1.91 \pm 0.24) * 10^{-8}$ ergs/cm³/sec/100 sfu. The latitudinal distribution
427 of peak emission rate and its correlation with the solar cycle is then presented for 21 latitudinal regions. Latitudinal correlation
428 analysis shows that the peak OH airglow emission is significantly correlated with the solar cycle at every latitude from 50°S
429 to 50°N, except for the equatorial region. The solar response distribution of the peak OH airglow emission shows a strong
430 south-north asymmetry between the two hemispheres, with the solar response in the southern hemisphere being higher than
431 that of the corresponding latitude in the northern hemisphere. The solar response is weakest in the equatorial region. The
432 standard deviation of the solar response in each hemisphere increases gradually from 30° to the equator and the poles.

433

434 *Code availability.* The code is available at <http://www.doi.org/10.57760/sciencedb.space.00659>.

435

436 *Data availability.* The OH airglow data can be accessed via <https://saber.gats-inc.com>. The MERRA-2 data
437 (MERRA2_300.tavg_) can be accessed via <http://disc.gsfc.nasa.gov>. The F_{10.7} data can be accessed via
438 <https://omniweb.gsfc.nasa.gov/form/dx1.html>.

439



440 *Author contributions.* DW processed and analyzed the data and wrote the manuscript; SYG, YFW, and LT reviewed and edited
441 the manuscript.

442
443 *Competing interests.* The authors declare that they have no conflict of interest.

444
445 *Acknowledgements.* This work was performed in the framework of space physics research (SPR). We are very grateful to the
446 SABER team for providing the airglow data. We thank NASA for the MERRA-2 wind field data and $F_{10.7}$ data.

447
448 *Financial support.* This research has been supported by the National Natural Science Foundation of China (grant nos. 41831071
449 and 42188101).

450
451

452 **References**

453 Abreu, V. J. and Yee, J. H.: DIURNAL AND SEASONAL-VARIATION OF THE NIGHTTIME OH (8-3) EMISSION AT
454 LOW LATITUDES, *J. Geophys. Res.-Space Phys.*, 94, 11949-11957, 10.1029/JA094iA09p11949, 1989.

455 Baker, D. J., Thurgood, B. K., Harrison, W. K., Mlynczak, M. G., and Russell, J. M.: Equatorial enhancement of the nighttime
456 OH mesospheric infrared airglow, *Physica Scripta*, 75, 615-619, 10.1088/0031-8949/75/5/004, 2007.

457 Batista, P. P., Takahashi, H., and Clemesha, B. R.: SOLAR-CYCLE AND THE QBO EFFECT ON THE MESOSPHERIC
458 TEMPERATURE AND NIGHTGLOW EMISSIONS AT A LOW-LATITUDE STATION, in: *Earths Middle Atmosphere*,
459 edited by: Grose, W. L., Ghazi, A., Geller, M. A., and Shepherd, G. G., *Advances in Space Research*, 9, Pergamon Press Ltd,
460 Oxford, 221-224, 10.1016/0273-1177(94)90139-2, 1994.

461 Buriti, R. A., Takahashi, H., Gobbi, D., de Medeiros, A. F., Nepomuceno, A. A., and Lima, L. M.: Semiannual oscillation of
462 the mesospheric airglow at 7.4 degrees S during the PSMOS observation period of 1998-2001, *J. Atmos. Sol.-Terr. Phys.*, 66,
463 567-572, 10.1016/j.jastp.2004.01.009, 2004.

464 Burrage, M. D., Hagan, M. E., Skinner, W. R., Wu, D. L., and Hays, P. B.: LONG-TERM VARIABILITY IN THE SOLAR
465 DIURNAL TIDE OBSERVED BY HRDI AND SIMULATED BY THE GSWM, *Geophys. Res. Lett.*, 22, 2641-2644,
466 10.1029/95gl02635, 1995.

467 Burrage, M. D., Vincent, R. A., Mayr, H. G., Skinner, W. R., Arnold, N. F., and Hays, P. B.: Long-term variability in the
468 equatorial middle atmosphere zonal wind, *J. Geophys. Res.-Atmos.*, 101, 12847-12854, 10.1029/96jd00575, 1996.

469 Clemesha, B., Takahashi, H., Simonich, D., Gobbi, D., and Batista, P.: Experimental evidence for solar cycle and long-term
470 change in the low-latitude MLT region, *J. Atmos. Sol.-Terr. Phys.*, 67, 191-196, 10.1016/j.jastp.2004.07.027, 2005.



- 471 Deutsch, K. A. and Hernandez, G.: Long-term behavior of the OI 558 nm emission in the night sky and its aeronomical
472 implications, *J. Geophys. Res-Space Phys.*, 108, 10.1029/2002ja009611, 2003.
- 473 Gao, H., Xu, J., and Chen, G.-M.: The responses of the nightglow emissions observed by the TIMED/SABER satellite to solar
474 radiation, *Journal of Geophysical Research: Space Physics*, 121, 1627-1642, <https://doi.org/10.1002/2015JA021624>, 2016.
- 475 Gao, H., Xu, J. Y., and Wu, Q. A.: Seasonal and QBO variations in the OH nightglow emission observed by TIMED/SABER,
476 *J. Geophys. Res-Space Phys.*, 115, 13, 10.1029/2009ja014641, 2010.
- 477 Huang, T. Y.: Simulations of airglow variations induced by the CO₂ increase and solar cycle variation from 1980 to 1991, *J.*
478 *Atmos. Sol.-Terr. Phys.*, 147, 138-147, 10.1016/j.jastp.2016.07.014, 2016.
- 479 Laskar, F. I., Pallamraju, D., and Veenadhari, B.: Vertical coupling of atmospheres: dependence on strength of sudden
480 stratospheric warming and solar activity, *Earth Planets and Space*, 66, 10.1186/1880-5981-66-94, 2014.
- 481 Laskar, F. I., Pallamraju, D., Lakshmi, T. V., Reddy, M. A., Pathan, B. M., and Chakrabarti, S.: Investigations on vertical
482 coupling of atmospheric regions using combined multiwavelength optical dayglow, magnetic, and radio measurements, *Journal*
483 *of Geophysical Research: Space Physics*, 118, 4618-4627, <https://doi.org/10.1002/jgra.50426>, 2013.
- 484 Liu, G. and Shepherd, G. G.: An empirical model for the altitude of the OH nightglow emission, *Geophys. Res. Lett.*, 33,
485 10.1029/2005gl025297, 2006.
- 486 Lopez-Gonzalez, M. J., Rodriguez, E., Wiens, R. H., Shepherd, G. G., Sargoytchev, S., Brown, S., Shepherd, M. G., Aushev,
487 V. M., Lopez-Moreno, J. J., Rodrigo, R., and Cho, Y. M.: Seasonal variations of O-2 atmospheric and OH(6-2) airglow and
488 temperature at mid-latitudes from SATI observations, *Ann. Geophys.*, 22, 819-828, 10.5194/angeo-22-819-2004, 2004.
- 489 Marsh, D. R., Smith, A. K., Mlynczak, M. G., and Russell, J. M.: SABER observations of the OH Meinel airglow variability
490 near the mesopause, *J. Geophys. Res-Space Phys.*, 111, 14, 10.1029/2005ja011451, 2006.
- 491 Melo, S. M. L., Lowe, R. P., and Takahashi, H.: The nocturnal behavior of the hydroxyl airglow at the equatorial and low
492 latitudes as observed by WINDII: Comparison with ground-based measurements, *J. Geophys. Res-Space Phys.*, 104, 24657-
493 24665, 10.1029/1999ja900291, 1999.
- 494 Mulligan, F. J., Horgan, D. F., Galligan, J. G., and Griffin, E. M.: MESOPAUSE TEMPERATURES AND INTEGRATED
495 BAND BRIGHTNESSES CALCULATED FROM AIRGLOW OH EMISSIONS RECORDED AT MAYNOOTH (53.2-
496 DEGREES-N, 6.4-DEGREES-W) DURING 1993, *J. Atmos. Terr. Phys.*, 57, 1623-1637, 10.1016/0021-9169(94)00133-9,
497 1995.
- 498 Newman, P. A., Coy, L., Pawson, S., and Lait, L. R.: The anomalous change in the QBO in 2015-2016, *Geophys. Res. Lett.*,
499 43, 8791-8797, 10.1002/2016gl070373, 2016.
- 500 Pertsev, N. and Perminov, V.: Response of the mesopause airglow to solar activity inferred from measurements at Zvenigorod,
501 Russia, *Ann. Geophys.*, 26, 1049-1056, 10.5194/angeo-26-1049-2008, 2008.
- 502 Pramitha, M., Kumar, K. K., Ratnam, M. V., Praveen, M., and Bhaskara Rao, S. V.: Stratospheric Quasi Biennial Oscillation
503 Modulations of Migrating Diurnal Tide in the Mesosphere and Lower Thermosphere Over the Low and Equatorial Latitudes,
504 *J. Geophys. Res-Space Phys.*, 126, 10.1029/2020ja028970, 2021.



- 505 Reid, I. M., Spargo, A. J., and Woithe, J. M.: Seasonal variations of the nighttime O(1S) and OH (8-3) airglow intensity at
506 Adelaide, Australia, *J. Geophys. Res.-Atmos.*, 119, 6991-7013, [10.1002/2013jd020906](https://doi.org/10.1002/2013jd020906), 2014.
- 507 Russell, J. P. and Lowe, R. P.: Atomic oxygen profiles (80-94 km) derived from Wind Imaging Interferometer/Upper
508 Atmospheric Research Satellite measurements of the hydroxyl airglow: 1. Validation of technique, *J. Geophys. Res.-Atmos.*,
509 108, [10.1029/2003jd003454](https://doi.org/10.1029/2003jd003454), 2003.
- 510 Scheer, J., Reisin, E. R., and Mandrini, C. H.: Solar activity signatures in mesopause region temperatures and atomic oxygen
511 related airglow brightness at El Leoncito, Argentina, *J. Atmos. Sol.-Terr. Phys.*, 67, 145-154,
512 <https://doi.org/10.1016/j.jastp.2004.07.023>, 2005.
- 513 Shepherd, M. G., Liu, G. P., and Shepherd, G. G.: Mesospheric semiannual oscillation in temperature and nightglow emission,
514 *J. Atmos. Sol.-Terr. Phys.*, 68, 379-389, [10.1016/j.jastp.2005.02.029](https://doi.org/10.1016/j.jastp.2005.02.029), 2006.
- 515 Takahashi, H., Clemesha, B. R., and Batista, P. P.: PREDOMINANT SEMI-ANNUAL OSCILLATION OF THE UPPER
516 MESOSPHERIC AIRGLOW INTENSITIES AND TEMPERATURES IN THE EQUATORIAL REGION, *J. Atmos. Terr.*
517 *Phys.*, 57, 407-414, [10.1016/0021-9169\(94\)e0006-9](https://doi.org/10.1016/0021-9169(94)e0006-9), 1995.
- 518 Tang, C., Wu, B., Wei, Y., Qing, C., Dai, C., Li, J., and Wei, H.: The Responses of Ozone Density to Solar Activity in the
519 Mesopause Region and the Mutual Relationship Based on SABER Measurements During 2002–2016, *Journal of Geophysical*
520 *Research: Space Physics*, 123, 3039-3049, <https://doi.org/10.1002/2017JA025126>, 2018.
- 521 Taylor, M. J., Taori, A. K., Hatch, D. R., Liu, H. L., and Roble, R. G.: Characterization of the semi-annual-oscillation in
522 mesospheric temperatures at low-latitudes, in: *Coupling Processes in the Mlt Region*, edited by: Clemesha, B., and Taylor, M.,
523 *Advances in Space Research*, 11, Elsevier Science Ltd, Oxford, 2037-2043, [10.1016/j.asr.2005.05.111](https://doi.org/10.1016/j.asr.2005.05.111), 2005.
- 524 von Savigny, C.: Variability of OH(3-1) emission altitude from 2003 to 2011: Long-term stability and universality of the
525 emission rate-altitude relationship, *J. Atmos. Sol.-Terr. Phys.*, 127, 120-128, [10.1016/j.jastp.2015.02.001](https://doi.org/10.1016/j.jastp.2015.02.001), 2015.
- 526 Wiens, R. H. and Weill, G.: Diurnal, annual and solar cycle variations of hydroxyl and sodium nightglow intensities in the
527 Europe-Africa sector, *Planetary and Space Science*, 21, 1011-1027, [https://doi.org/10.1016/0032-0633\(73\)90147-5](https://doi.org/10.1016/0032-0633(73)90147-5), 1973.
- 528 Xu, J., Smith, A. K., Liu, H.-L., Yuan, W., Wu, Q., Jiang, G., Mlynczak, M. G., Russell III, J. M., and Franke, S. J.: Seasonal
529 and quasi-biennial variations in the migrating diurnal tide observed by Thermosphere, Ionosphere, Mesosphere, Energetics
530 and Dynamics (TIMED), *Journal of Geophysical Research: Atmospheres*, 114, <https://doi.org/10.1029/2008JD011298>, 2009.
- 531 Yee, J. H., Crowley, G., Roble, R. G., Skinner, W. R., Burrage, M. D., and Hays, P. B.: Global simulations and observations
532 of O(S-1), O-2((1)Sigma) and OH mesospheric nightglow emissions, *J. Geophys. Res-Space Phys.*, 102, 19949-19968,
533 [10.1029/96ja01833](https://doi.org/10.1029/96ja01833), 1997.
- 534 Zaragoza, G., Taylor, F. W., and Lopez-Puertas, M.: Latitudinal and longitudinal behavior of the mesospheric OH nightglow
535 layer as observed by the Improved Stratospheric and Mesospheric Sounder on UARS, *J. Geophys. Res.-Atmos.*, 106, 8027-
536 8033, [10.1029/2000jd900633](https://doi.org/10.1029/2000jd900633), 2001.
- 537